

Ultrafast, Controllable Synthesis of Sub-Nano Metallic Clusters through Defect Engineering

Yonggang Yao,^{†,‡} Zhennan Huang,^{†,§} Pengfei Xie,^{†,‡} Tangyuan Li,^{‡,†} Steven D. Lacey,^{‡,ⓑ} Miaolun Jiao,[‡] Hua Xie,[‡] Kun Kelvin Fu,[‡] Rohit Jiji Jacob,^{||} Dylan Jacob Kline,^{||,ⓑ} Yong Yang,^{||,ⓑ} Michael R. Zachariah,^{||,ⓑ} Chao Wang,^{*,‡,ⓑ} Reza Shahbazian-Yassar,^{*,§,ⓑ} and Liangbing Hu^{*,‡,ⓑ}

[‡]Department of Materials Science and Engineering, University of Maryland, College Park, Maryland 20742, United States

[§]Department of Mechanical and Industrial Engineering, University of Illinois at Chicago, 842 West Taylor Street, Chicago, Illinois 60607, United States

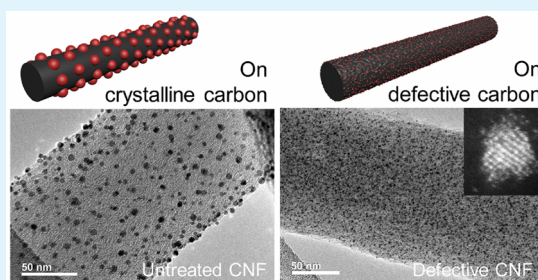
[†]Department of Chemical and Biomolecular Engineering, Johns Hopkins University, Baltimore, Maryland 21218, United States

^{||}Department of Chemical and Biomolecular Engineering and Chemistry and Biochemistry, University of Maryland, College Park, Maryland 20742, United States

Supporting Information

ABSTRACT: Supported metallic nanoclusters (NCs, < 2 nm) are of great interests in various catalytic reactions with enhanced activities and selectivities, yet it is still challenging to efficiently and controllably synthesize ultrasmall NCs with a high-dispersal density. Here we report the in situ synthesis of surfactant-free, ultrasmall, and uniform NCs via a rapid thermal shock on defective substrates. This is achieved by using high-temperature synthesis with extremely fast kinetics while limiting the synthesis time down to milliseconds (e.g., ~1800 K for 55 ms) to avoid aggregation. Through defect engineering and optimized loading, the particle size can be robustly tuned from >50 nm nanoparticles to <1 nm uniform NCs with a high-dispersal density. We demonstrate that the ultrasmall NCs exhibit drastically improved activities for catalytic CO oxidation as compared to their nanoparticulated counterparts. In addition, the reported method shows generality in synthesizing most metallic NCs (e.g., Pt, Ru, Ir, Ni) in an extremely facile and efficient manner. The ultrafast and controllable synthesis of uniform, high-density, and size-controllable NCs paves the way for the utilization and nanomanufacturing of NCs for a range of catalytic reactions.

KEYWORDS: nanoclusters, high-density dispersion, defects, thermal shock, CO oxidation



INTRODUCTION

Heterogeneous catalysts are ubiquitously used in catalytic reactions with industrial importance.^{1–10} Their catalytic activities are largely dependent on the particle size and dispersion density, which determines the total active surface area for catalytic reactions to occur. Supported metallic nanoclusters (NCs, <2 nm), and specifically ultrasmall NCs (≤1 nm), possess a high surface/volume ratio with most atoms exposed to the surface (i.e., with a low coordination), demonstrating improved catalytic activities as well as selectivities toward various reactions.^{1,2,4,5,8,9,11–13} However, those low-atomicity NCs have a strong tendency to aggregate to reduce their surface energy, and stabilization is critical for their practical applications. In addition, when the particle size is as small as ~1 nm, the delicate size control usually renders tedious synthesis procedures. The wide application of ultrafine NCs is therefore largely dependent on developing an efficient synthesis method that can stabilize the NCs, with the capabilities of robust control and potentials for scalable manufacturing.

Although wet-chemical colloidal processes can ex situ synthesize uniform, small and well-controlled NCs using surfactants and ligands, the subsequent dispersions of NCs uniformly onto supports and removal of ligands represent a grand challenge.^{3,6,10,14} Alternatively, supported NCs can be in situ synthesized via gas phase soft landing through mass selection^{4,5} or wet impregnation.^{1,2,9,14–16} Yet the soft landing technique often requires sophisticated equipment and is limited in scalability, whereas the impregnation method usually yields nanoparticles with a broad size distribution because of particle agglomeration during the prolonged thermal sintering (several hours).^{8,15,17} Recent studies were able to achieve uniform and small NCs in select systems by deliberate precursor designs, such as applying site-confining precursors using organometallic compounds^{3,7,9,18,19} or designing strong coordination between the precursor salt and the substrate.^{1,8,20} However, the sophisticated precursor design limits their

Received: April 24, 2019

Accepted: July 29, 2019

Published: July 29, 2019

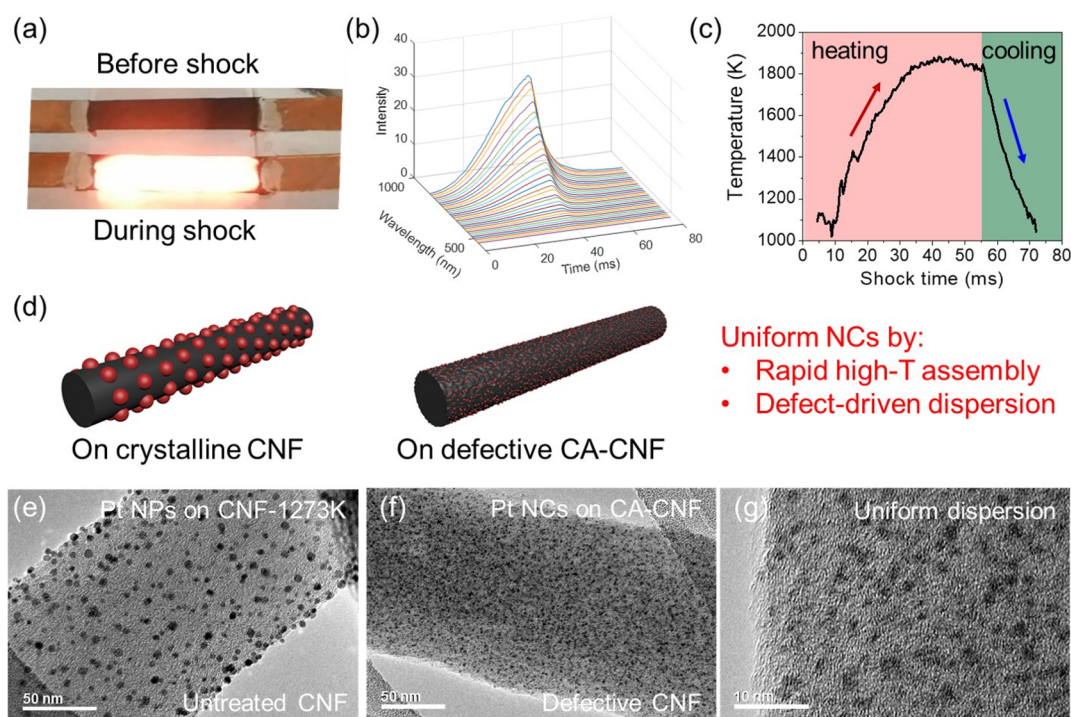


Figure 1. Rapid NC dispersion via the thermal shock process on defective carbon. (a) Photo images of samples before and during the high-temperature shock process. The emitted light indicates high temperature reached in the sample. (b) Emitted light spectra and (c) temperature evolution during thermal shock. (d) Schematic to demonstrate the role of defects on the particle size and dispersion. TEM images of (e) Pt nanoparticles on untreated CNF-1273K and (f, g) Pt NCs on defective CA-CNF synthesized with the same shock parameters and precursor loading ($0.5 \mu\text{mol}/\text{cm}^2$).

generality and the followed reduction/sintering process (hours to days) still renders low efficiency and potential cluster agglomeration.^{21–23}

Herein, we report the in situ, high temperature synthesis of clean, ultrasmall, and uniformly dispersed NCs using a rapid thermal shock on defective substrates. The thermal shock synthesis with a duration down to milliseconds renders a superior production efficiency and at the same time avoids cluster aggregation. In addition, surface defects on the substrate are critical to effectively disperse and stabilize the NCs. The particle size can be tailored from >50 nm nanoparticles to <1 nm NCs with a high-dispersal density through defect engineering and optimizing precursor loading. The reported method can be generally applied to a wide range of metallic NCs (e.g., Pt, Ru, Ir, Ni). The synthesis of ultrasmall NCs via this thermal shock method demonstrates superior advantages as a facile, rapid, and general process for in situ, high-density dispersion of size-controllable NCs for various catalytic applications.

RESULTS AND DISCUSSION

In a typical experiment, ethanol-based salt precursors are uniformly deposited on defective carbon substrate, followed by a high temperature thermal shock triggered by electrical Joule heating, leading to the in situ decomposition of the salt precursors and nucleation of ultrasmall NCs. In the high temperature shock process, the material emits visible light due to the high temperature induced radiation (Figure 1a), and the emitted light spectra can be collected to estimate the temperature evolution during synthesis (Figure 1b, see details in Methods). The peak temperature reaches ~ 1800 K within a heating period of ~ 55 ms followed by rapid quenching at a rate

of $\sim 1 \times 10^4$ K/s (Figure 1c). This highly controllable and rapid heating is critical for efficient production and nanocluster formation. Besides the heating parameters, the surface defects of the carbon support act as the nucleation and dispersion sites for nanoclusters in the thermal shock synthesis. As schematically shown in Figure 1d, carbon supports with a high crystallinity (i.e., lack of surface defects) lead to large nanoparticles because of particle aggregation at high temperature. In contrast, defective carbon surfaces can help disperse and stabilize metal clusters to prevent agglomeration and achieve a high-density distribution.

We chose Pt as the proof of concept for this study and extended our analysis to other elements to demonstrate the generality of this technique. Carbon nanofibers were used as carbon supports because of their simple fiber structure and easily precursor loading. We believe other defective carbon substrates, such as reduced graphene oxides,²⁴ holey graphene,^{25,26} and N-doped carbon,^{27,28} could also be used for particle dispersion with a similar mechanism. Pt was synthesized on both untreated CNF (CNF carbonized at 1273K, CNF-1273K) and defective CNF (CO_2 activated CNF, CA-CNF) using the same precursor loading ($0.5 \mu\text{mol}/\text{cm}^2$, Figure S1) and shock process. Although the Pt nanoparticles on the CNF-1273K are sparsely distributed (Figure 1e), the same process yields more uniform and densely packed Pt NCs on the defective CA-CNFs (Figure 1f, g). As the only difference among these samples is the defect concentrations (untreated CNF-1273K vs. defective CA-CNF), we can conclude that defects on the carbon play a key role in particle dispersion during the thermal shock process. Therefore, by combining rapid thermal shock with the defective substrate, we

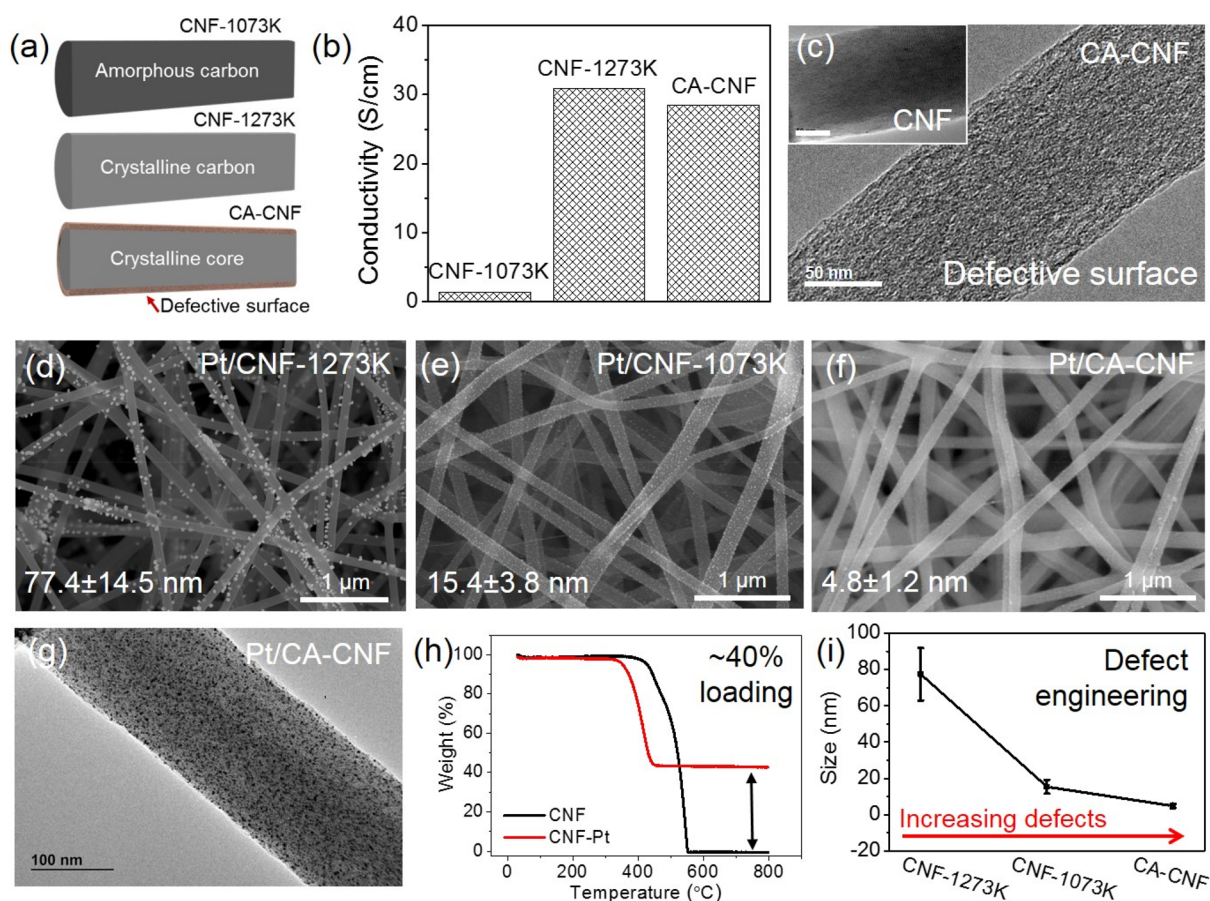


Figure 2. Particle size control via defect engineering. (a) Schematic for CNFs with different defect concentrations: CNF-1073K, CNF-1273K and CA-CNF (first carbonized at 1273K and then thermally activated by CO_2). (b) Conductivity for different CNFs. (c) TEM image of CA-CNF, showing the defective surface with meso- and micro- pores. The inset shows the smooth surface of a bare CNF-1273K before CO_2 activation. (d–f) SEM images of Pt dispersed on CNF-1273K, CNF-1073K, and CA-CNFs, respectively (loading $5 \mu\text{mol}/\text{cm}^2$). (g) TEM images of high-density, well-dispersed Pt nanoparticles on CA-CNF after thermal shock. (h) Particle loading measured by TGA measurement. (i) Summary of particle size control through defect engineering.

are able to synthesize uniformly small NCs in an extremely efficient manner.

The role of defects in particle dispersion was further studied and employed for size control. CNF substrates with different defect concentrations were used for synthesis, specifically, CNF carbonized at 1073 K (CNF-1073K), 1273 K (CNF-1273K), and defective CA-CNF (Figure 2a). We first elucidated the defect levels of these CNF substrates revealed by their conductivity (Figure 2b). For CNF-1073K, the carbon nanofibers were carbonized at a low temperature (1073 K), which renders CNF with an amorphous structure and a lot of defects, leading to a poor conductivity. In contrast, the CNF-1273K carbonized at a higher temperature (1273 K) has a more crystalline structure with less defects, leading to a higher conductivity. Then the 1273K carbonized fibers was further treated by the CO_2 thermal activation process to create CA-CNF with a defective surface and slightly decreased conductivity. In addition, we used X-ray photoelectron spectroscopy (XPS), wetting angle, and Raman measurements^{29,30} to determine the defect levels (Figure S2). The CO_2 activation process generates a high surface area, defective surface on the more crystalline carbon core.^{31–33} Figure 2c is a TEM image of the CA-CNF sample, which exhibits a defective and rugged surface with numerous meso- and micropores created during the CO_2 activation process ($\text{C} + \text{CO}_2 = 2\text{CO}\uparrow$

leads to C vacancies and pores).^{31,33–35} In contrast, the TEM image of an untreated CNF-1273K shows a relatively smooth surface (Figure 2c inset). The crystalline core enables better conductivity for electrical Joule heating while the surface pores and defects in CA-CNF are critical for later particle dispersion and stabilization.³⁶

We then synthesized Pt particles on these three types of CNF substrates using a precursor loading of $5 \mu\text{mol}/\text{cm}^2$ and the same thermal shock process. The higher loading renders larger particles and enables direct comparison of the samples by nondestructive scanning electron microscopy (SEM). Figure 2d–f and Figure S3 show the SEM images of Pt nanoparticles on CNF-1273K, CNF-1073K, and CA-CNFs. Distinct Pt size and uniformity differences were apparent on these substrates: from substantially larger nanoparticles on the untreated CNF-1273K ($77.4 \text{ nm} \pm 14.5 \text{ nm}$), to smaller nanoparticles on CNF-1073K ($15.4 \text{ nm} \pm 3.8 \text{ nm}$), and finally, the CA-CNF sample produces the smallest particle distribution ($4.8 \text{ nm} \pm 1.2 \text{ nm}$, Figure 2g) with high-density dispersion across the 3D tortuous support, which thermal gravimetric analysis (TGA) confirmed to be $\sim 40 \text{ wt} \%$ (Figure 2h). These results indicate the critical role of defects in CNF substrates on the final particle size distribution, in which smaller particle sizes and greater density derive from a higher number of substrate defects (Figure 2i).

The particle size can be further tuned by optimizing the precursor loading. By decreasing the loading of Pt precursors from $5 \mu\text{mol}/\text{cm}^2$ to 0.5 and $0.1 \mu\text{mol}/\text{cm}^2$, the particle size can be substantially decreased from $4.8 \pm 1.2 \text{ nm}$ to roughly $\sim 1.7 \text{ nm}$ and $\sim 0.8 \text{ nm}$, respectively (Figure 3 and Figures S4

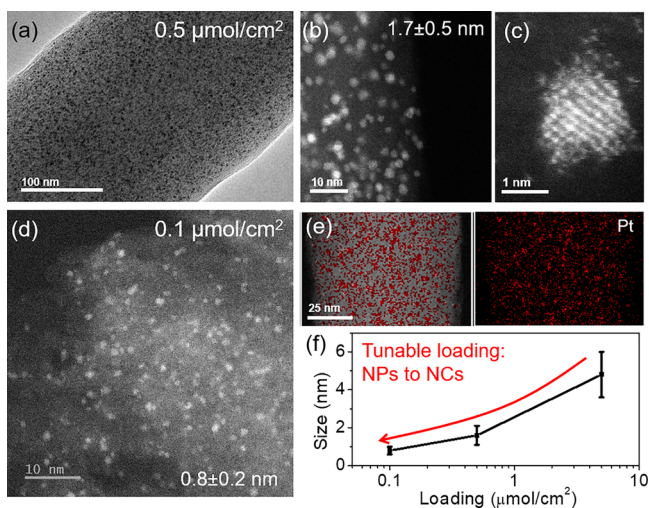


Figure 3. Ultrasmall Pt NCs on CA-CNFs with optimized loading. (a) TEM and (b, c) high-angle annular dark-field (HAADF) images of high-density NCs on CA-CNFs with a precursor loading of $0.5 \mu\text{mol}/\text{cm}^2$. The ultrasmall NC shows a low-coordination packing of atoms. (d–e) HAADF image of high-density subnanometer NCs on CA-CNFs with a precursor loading of $0.1 \mu\text{mol}/\text{cm}^2$. An even small size distribution was achieved. (e) EDS maps and a representative spectrum confirm the uniform dispersion of Pt NCs on the CA-CNFs. (f) Particle size distribution tuned by the initial precursor loading.

and S5). Importantly, these ultrasmall NCs demonstrate loosely packed surface atoms (i.e., with a low-coordination, Figure 3c) because of the ultrasmall configuration that lacks

the cohesive energy for atom condensation. Meanwhile, the high-density dispersion is still maintained despite the drastically decreased Pt loading (Figure 3d). The energy-dispersive spectroscopy (EDS) was also performed on the ultrasmall NC sample, which confirmed a uniform elemental distribution of Pt across the CA-CNF support (Figure 3e). The loosely packed NCs with a high surface area could facilitate active surfaces for various catalytic applications.

We also compared the size and dispersal density of the NCs prepared in this work to typical sizes reported in the literature (Table S1), in which the NCs synthesized by our facile and rapid thermal shock method are among the highest dispersal density reported to date.^{6–8,17} This is because the rapid thermal shock method is a high temperature dispersion can drive the rapid moving of metallic NCs at high temperature to maximize the defect occupation. By optimizing or tuning the initial precursor loading, the metal dispersion can be tuned from nanoparticles to NCs uniformly distributed across the CA-CNFs (Figure 3f).

We evaluated the catalytic performance of the ultrafine NCs on CA-CNFs for the CO oxidation reaction, and the result was compared with the larger sized nanoparticles (NPs) with the same Pt loading ($0.5 \mu\text{mol}/\text{cm}^2$). Note that the morphology of the Pt NPs and NCs can be found in Figure 1e, f. As shown in Figure 4a, the Pt NCs on CA-CNFs possessed 50% CO conversion at $136 \text{ }^\circ\text{C}$, which was lower than that temperature of Pt NPs ($209 \text{ }^\circ\text{C}$). Also, complete CO oxidation occurred at $150 \text{ }^\circ\text{C}$ for the Pt NCs on CA-CNFs, which was strikingly lower than that for Pt NPs ($226 \text{ }^\circ\text{C}$). Additionally, bare CA-CNFs were also tested for CO oxidation to clarify the potential contribution of defects on CA-CNFs to the reaction.

As shown in Figure 4a, the bare CA-CNF substrates showed negligible CO conversion in the measured temperature range, demonstrating that Pt NCs serves as the active sites for CO conversion in the Pt NCs sample. Moreover, the Arrhenius plot (the logarithm of reaction rate versus inverse temperature)

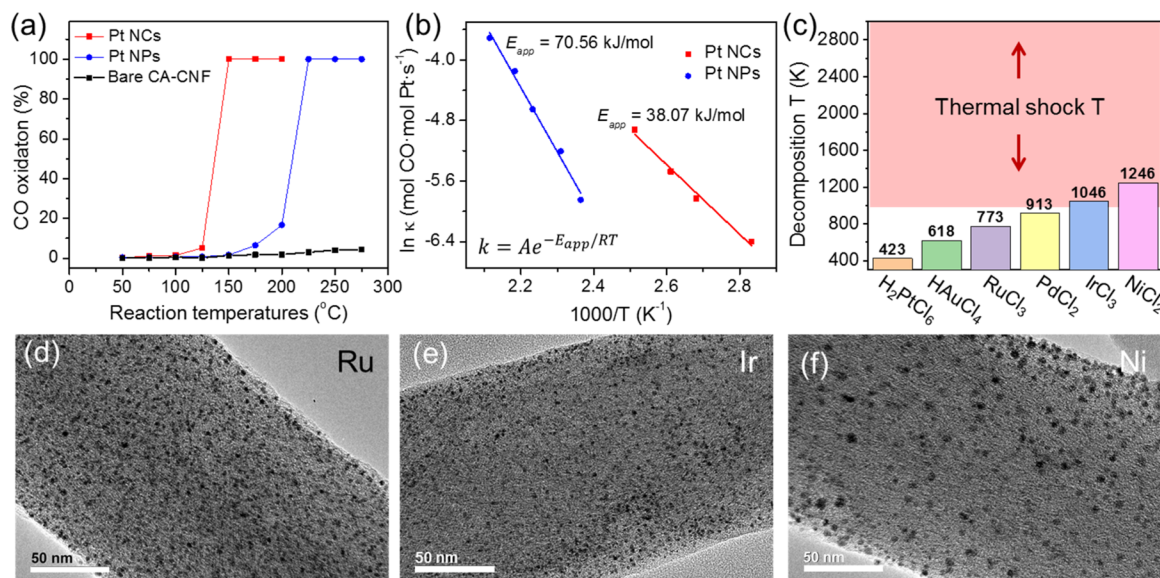


Figure 4. Catalytic CO oxidation and universality of thermal-shock-synthesized NCs. (a) CO oxidation reaction catalyzed by bare CA-CNFs, Pt nanoparticles (Pt-NPs), and Pt NCs, showing different catalytic activities due to the size effect. (b) The corresponding Arrhenius plot for CO oxidation by the Pt NPs and NCs, showing different apparent activation energies (E_{app}). (c) The thermal shock temperature is much higher than various salt precursors' thermal decomposition temperatures, which ensures the generality for synthesizing of most metal NCs, (d–f) as shown for Ru, Ir, and Ni on CA-CNFs ($0.5 \mu\text{mol}/\text{cm}^2$).

of the catalytic process shows a linear relation (Figure 4b), indicating a typical rate-limited thermally activation process. We therefore derived the apparent activation energy (E_{app}) in CO oxidation reaction for Pt NCs to be 38.07 kJ/mol, which is much smaller than the value obtained for Pt NPs (70.56 kJ/mol). The performance difference may be attributed to the significantly increased active surface (and therefore active sites) in the ultrafine Pt NCs as compared to nanoparticles (i.e., size effect) for catalytic CO oxidation.^{37–42} We also confirmed that these ultrafine nanoclusters are still well dispersed after the catalytic reaction, indicating a good thermal stability (Figure S6).

Because the temperature range for thermal shock is higher than the salt precursors' thermal decomposition temperatures (Figure 4c), in theory, nearly any metallic NC can be produced using this facile physical synthesis method. Figures 4d–f show the synthesis of Ru, Ir, and Ni NCs on CA-CNFs using 0.5 $\mu\text{mol}/\text{cm}^2$ precursorloading, and the uniform NCs formation in all metals were achieved. Therefore, the thermal shock method offers a robust, efficient and general synthetic route for ultrafine and well-dispersed NCs.

CONCLUSION

In summary, we report the in situ synthesis of ultras-small and high-density NCs using a facile and rapid thermal shock method on the defective supports. By limiting particle synthesis duration down to milliseconds, the thermal shock process enables rapid production of ultras-small NCs via brief high temperature exposure to avoid particle coarsening. In the meantime, the surface defects act as nucleation sites and help stabilize and disperse these NCs from aggregating. Accordingly, robust tunability from >50 nm nanoparticles to <1 nm NCs is readily achieved using surface-treated carbon supports and optimizing the precursor salt loading. The ultras-small and high-density NCs showed drastically improved catalytic activity in the CO oxidation reaction as compared with their nanoparticle counterparts. The reported method demonstrates generality in synthesizing most metallic nanoclusters in an extremely facile and efficient manner. These ultras-small and uniform nanoclusters are expected to be utilized in a range of applications, including electrochemistry and heterogeneous catalysis.

METHODS

Carbon Nanofiber Preparation. Nanofibers were synthesized by electrospinning of polyacrylonitrile (Sigma-Aldrich) in dimethylformamide (Sigma-Aldrich) solution (8 wt %). The nanofiber mat was pretreated in air at 533 K for 5 h followed by carbonization at 1073K (CNF-1073K) and 1273K (CNF-1273K) for 2 h in Ar. The CNF-1273K material can then be thermally annealed under a CO_2 atmosphere (80 mL/min) at 1023K for 3 h to obtain CA-CNF.

Metal Salt Loading and Thermal Shock. The salt precursors were dissolved in ethanol-based solutions at different concentrations (0.05, 0.005, and 0.001 mol/L), and the solutions were dipped onto the above CNF films ($\sim 100\text{--}120 \mu\text{L}/\text{cm}^2$). The salt precursor-loaded CNF films were subjected to high temperature thermal shock in the glovebox by applying an electrical pulse of 55 ms duration using a Keithley 2425. In a typical CA-CNF sample, the input power density is 40–60 W/cm^2 to achieve high-temperature heating and is adjusted accordingly with their respective resistances. The temperature was monitored by a time-resolved pyrometer for ultrafast spectrum collection.¹³

Structural Characterization. The morphology was characterized by SEM (Hitachi SU-70 FEG-SEM at 10 kV) and TEM (JEOL 2100F FEG TEM, and JEOL TEM/STEM ARM 200CF). Raman spectroscopy

data was performed on a Horiba Jobin-Yvon and the XPS work was carried out on a Kratos Axis 165. TGA was performed on a TGA 550 from TA Instruments.

CO Oxidation Evaluation. Catalytic CO conversion was conducted in a fixed-bed flow reactor at atmospheric pressure. 15–20 mg of catalyst was loaded into a quartz tube reactor (7 mm i.d.) and pretreated in He and left to cool to 50 °C. The gas flow was then switched to a reactant gas feed (50 mL/min) with 1% CO and 4% O_2 and rest is He. The CO measurement was test from 50 to 275 °C with a 25 °C step interval and a heating rate of 5 °C/min. The sample was equilibrated for at least 30 min before measurement and each measurement take ~ 10 min to finish. Fourier-transform infrared spectrometer (Nicolet 6700) were used to analyze CO at 2173 cm^{-1} and the conversions were estimated using the following equation:

$$\text{CO conversion} = \frac{[\text{CO}]_{\text{inlet}} - [\text{CO}]_{\text{outlet}}}{[\text{CO}]_{\text{inlet}}} 100\%$$

ASSOCIATED CONTENT

Supporting Information

The Supporting Information is available free of charge on the ACS Publications website at DOI: 10.1021/acsami.9b07198.

Figures S1–S6 and Table S1 (PDF)

AUTHOR INFORMATION

Corresponding Authors

*Email: binghu@umd.edu.

*Email: rsyassar@uic.edu.

*Email: chaowang@jhu.edu.

ORCID

Steven D. Lacey: 0000-0003-1096-7699

Dylan Jacob Kline: 0000-0001-8800-2841

Yong Yang: 0000-0001-5169-1479

Michael R. Zachariah: 0000-0002-4115-3324

Chao Wang: 0000-0001-7398-2090

Reza Shahbazian-Yassar: 0000-0002-7744-4780

Liangbing Hu: 0000-0002-9456-9315

Author Contributions

L.H. and Y.Y. contributed to the idea and experimental design. Y.Y., T.L., S.L., M.J., H.X., and F.K. conducted the materials preparation and characterization. Z.H. and R.S.-Y. performed high-resolution microscope study. P.X. and C.W. contributed to the catalysis evaluation. R.J., D.K., Y.Y., and M.Z. performed the high-temperature characterization and thermal gravimetric analysis. L.H. and Y.Y. wrote the paper and all authors contributed to the writing.

Author Contributions

[†]Y.Y., Z.H., P.X., and T.L. contributed equally to this work.

Notes

The authors declare no competing financial interest.

ACKNOWLEDGMENTS

This work is funded by the National Science Foundation (1635221). We acknowledge the facility support from the Maryland Nanocenter, its Surface Analysis Center, and the AIMLab. R.S.Y. is thankful for the financial support from the NSF-DMR Award 1809439. P.X. and C.W. thank the financial support provided U.S. Department of Energy by the Advanced Research Projects Agency-Energy (ARPA-E, DE-AR0000952).

REFERENCES

- (1) Corma, A.; Concepción, P.; Boronat, M.; Sabater, M. J.; Navas, J.; Yacaman, M. J.; Larios, E.; Posadas, A.; López-Quintela, M. A.; Buceta, D.; Mendoza, E.; Guilera, G.; Mayoral, A. Exceptional Oxidation Activity with Size-Controlled Supported Gold Clusters of Low Atomicity. *Nat. Chem.* **2013**, *5*, 775–781.
- (2) Liu, Y.; Tsunoyama, H.; Akita, T.; Xie, S.; Tsukuda, T. Aerobic Oxidation of Cyclohexane Catalyzed by Size-Controlled Au Clusters on Hydroxyapatite: Size Effect in the Sub-2 Nm Regime. *ACS Catal.* **2011**, *1*, 2–6.
- (3) Astruc, D.; Boisselier, E.; Ornelas, C. Dendrimers Designed for Functions: From Physical, Photophysical, and Supramolecular Properties to Applications in Sensing, Catalysis, Molecular Electronics, Photonics, and Nanomedicine. *Chem. Rev.* **2010**, *110*, 1857–1959.
- (4) Vajda, S.; Pellin, M. J.; Greeley, J. P.; Marshall, C. L.; Curtiss, L. A.; Ballentine, G. A.; Elam, J. W.; Catillon-Mucherie, S.; Redfern, P. C.; Mehmood, F.; Zapol, P. Subnanometre Platinum Clusters as Highly Active and Selective Catalysts for the Oxidative Dehydrogenation of Propane. *Nat. Mater.* **2009**, *8*, 213–216.
- (5) Kaden, W. E.; Wu, T.; Kunkel, W. A.; Anderson, S. L. Electronic Structure Controls Reactivity of Size-Selected Pd Clusters Adsorbed on TiO₂ Surfaces. *Science* **2009**, *326*, 826–829.
- (6) Tan, Y.; Liu, X. Y.; Zhang, L.; Wang, A.; Li, L.; Pan, X.; Miao, S.; Haruta, M.; Wei, H.; Wang, H.; Wang, F.; Wang, X.; Zhang, T. ZnAl-Hydroxalite-Supported Au₂₅ Nanoclusters as Precatalysts for Chemoselective Hydrogenation of 3-Nitrostyrene. *Angew. Chem., Int. Ed.* **2017**, *56*, 2709–2713.
- (7) Shang, L.; Bian, T.; Zhang, B.; Zhang, D.; Wu, L.-Z.; Tung, C.-H.; Yin, Y.; Zhang, T. Graphene-Supported Ultrafine Metal Nanoparticles Encapsulated by Mesoporous Silica: Robust Catalysts for Oxidation and Reduction Reactions. *Angew. Chem.* **2014**, *126*, 254–258.
- (8) Wong, A.; Liu, Q.; Griffin, S.; Nicholls, A.; Regalbutto, J. R. Synthesis of Ultrasmall, Homogeneously Alloyed, Bimetallic Nanoparticles on Silica Supports. *Science* **2017**, *358*, 1427–1430.
- (9) Takahashi, M.; Koizumi, H.; Chun, W.-J.; Kori, M.; Imaoka, T.; Yamamoto, K. Finely Controlled Multimetallic Nanocluster Catalysts for Solvent-Free Aerobic Oxidation of Hydrocarbons. *Sci. Adv.* **2017**, *3*, No. e1700101.
- (10) Wilcoxon, J. P.; Abrams, B. L. Synthesis, Structure and Properties of Metal Nanoclusters. *Chem. Soc. Rev.* **2006**, *35*, 1162–1194.
- (11) Chen, M.; Goodman, D. W. Catalytically Active Gold: From Nanoparticles to Ultrathin Films. *Acc. Chem. Res.* **2006**, *39*, 739–746.
- (12) Hutchings, G. J. Heterogeneous Gold Catalysis. *ACS Cent. Sci.* **2018**, *4*, 1095–1101.
- (13) Yao, Y.; Huang, Z.; Xie, P.; Lacey, S. D.; Jacob, R. J.; Xie, H.; Chen, F.; Nie, A.; Pu, T.; Rehwoldt, M.; Yu, D.; Zachariah, M. R.; Wang, C.; Shahbazian-Yassar, R.; Li, J.; Hu, L. Carbothermal Shock Synthesis of High-Entropy-Alloy Nanoparticles. *Science* **2018**, *359*, 1489–1494.
- (14) Zhang, L.; Wang, E. Metal Nanoclusters: New Fluorescent Probes for Sensors and Bioimaging. *Nano Today* **2014**, *9*, 132–157.
- (15) Xie, S.; Tsunoyama, H.; Kurashige, W.; Negishi, Y.; Tsukuda, T. Enhancement in Aerobic Alcohol Oxidation Catalysis of Au₂₅ Clusters by Single Pd Atom Doping. *ACS Catal.* **2012**, *2*, 1519–1523.
- (16) Rodrigues, T. S.; Zhao, M.; Yang, T.-H.; Gilroy, K. D.; da Silva, A. G. M.; Camargo, P. H. C.; Xia, Y. Synthesis of Colloidal Metal Nanocrystals: A Comprehensive Review on the Reductants. *Chem. - Eur. J.* **2018**, *24*, 16944–16963.
- (17) Feng, J. J.; Chen, L. X.; Song, P.; Wu, X. L.; Wang, A. J.; Yuan, J. Bimetallic AuPd Nanoclusters Supported on Graphitic Carbon Nitride: One-Pot Synthesis and Enhanced Electrocatalysis for Oxygen Reduction and Hydrogen Evolution. *Int. J. Hydrogen Energy* **2016**, *41*, 8839–8846.
- (18) Sonoi, A.; Chun, W.-J.; Enoki, O.; Yamamoto, K.; Imaoka, T.; Takenaga, M.; Katoh, H. Size-Specific Catalytic Activity of Platinum Clusters Enhances Oxygen Reduction Reactions. *Nat. Chem.* **2009**, *1*, 397–402.
- (19) Bonanni, S.; Ait-Mansour, K.; Harbich, W.; Brune, H. Reaction-Induced Cluster Ripening and Initial Size-Dependent Reaction Rates for CO Oxidation on Ptn/TiO₂(110)-(1 × 1). *J. Am. Chem. Soc.* **2014**, *136*, 8702–8707.
- (20) Ding, K.; Cullen, D. A.; Zhang, L.; Cao, Z.; Roy, A. D.; Ivanov, I. N.; Cao, D. A General Synthesis Approach for Supported Bimetallic Nanoparticles via Surface Inorganometallic Chemistry. *Science* **2018**, *362*, 560–564.
- (21) Hansen, T. W.; Delariva, A. T.; Challa, S. R.; Datye, A. K. Sintering of Catalytic Nanoparticles: Particle Migration or Ostwald Ripening? *Acc. Chem. Res.* **2013**, *46*, 1720–1730.
- (22) Risse, T.; Shaikhutdinov, S.; Nilius, N.; Sterrer, M.; Freund, H. J. Gold Supported on Thin Oxide Films: From Single Atoms to Nanoparticles. *Acc. Chem. Res.* **2008**, *41*, 949–956.
- (23) Sehested, J.; Gelten, J. A. P.; Remedakis, I. N.; Bengaard, H.; Nørskov, J. K. Sintering of Nickel Steam-Reforming Catalysts: Effects of Temperature and Steam and Hydrogen Pressures. *J. Catal.* **2004**, *223*, 432–443.
- (24) Pei, S.; Cheng, H.-M. The Reduction of Graphene Oxide. *Carbon* **2012**, *50*, 3210–3228.
- (25) Lin, Y.; Liao, Y.; Chen, Z.; Connell, J. W. Holey Graphene: A Unique Structural Derivative of Graphene. *Mater. Res. Lett.* **2017**, *5*, 209–234.
- (26) Lacey, S. D.; Kirsch, D. J.; Li, Y.; Morgenstern, J. T.; Zarket, B. C.; Yao, Y.; Dai, J.; Garcia, L. Q.; Liu, B.; Gao, T.; Xu, S.; Raghavan, S. R.; Connell, J. W.; Lin, Y.; Hu, L. Extrusion-Based 3D Printing of Hierarchically Porous Advanced Battery Electrodes. *Adv. Mater.* **2018**, *30*, 1705651.
- (27) Gong, K.; Du, F.; Xia, Z.; Durstock, M.; Dai, L. Nitrogen-Doped Carbon Nanotube Arrays with High Electrocatalytic Activity for Oxygen Reduction. *Science* **2009**, *323*, 760–764.
- (28) Yao, Y.; Chen, F.; Nie, A.; Lacey, S. D.; Jacob, R. J.; Xu, S.; Huang, Z.; Fu, K.; Dai, J.; Salamanca-Riba, L.; Zachariah, M. R.; Shahbazian-Yassar, R.; Hu, L. In Situ High Temperature Synthesis of Single-Component Metallic Nanoparticles. *ACS Cent. Sci.* **2017**, *3*, 294–301.
- (29) Ferrari, A. C.; Basko, D. M. Raman Spectroscopy as a Versatile Tool for Studying the Properties of Graphene. *Nat. Nanotechnol.* **2013**, *8*, 235–246.
- (30) Yao, Y.; Fu, K. K.; Zhu, S.; Dai, J.; Wang, Y.; Pastel, G.; Chen, Y.; Li, T.; Wang, C.; Li, T.; Hu, L. Carbon Welding by Ultrafast Joule Heating. *Nano Lett.* **2016**, *16*, 7282–7289.
- (31) Chen, Y.; Liu, Q.; Wang, J. Carbon Dioxide Activated Carbon Nanofibers with Hierarchical Micro-/Mesoporosity towards Electrocatalytic Oxygen Reduction. *J. Mater. Chem. A* **2016**, *4*, 5553–5560.
- (32) Ju, X.; Liu, L.; Yu, P.; Guo, J.; Zhang, X.; He, T.; Wu, G.; Chen, P. Mesoporous Ru/MgO Prepared by a Deposition-Precipitation Method as Highly Active Catalyst for Producing CO_x-Free Hydrogen from Ammonia Decomposition. *Appl. Catal., B* **2017**, *211*, 167–175.
- (33) Song, H.; Xu, S.; Li, Y.; Dai, J.; Gong, A.; Zhu, M.; Zhu, C.; Chen, C.; Chen, Y.; Yao, Y.; Liu, B.; Song, J.; Pastel, G.; Hu, L. Hierarchically Porous, Ultrathick, “Breathable” Wood-Derived Cathode for Lithium-Oxygen Batteries. *Adv. Energy Mater.* **2018**, *8*, 1701203.
- (34) Chen, C.; Zhang, Y.; Li, Y.; Dai, J.; Song, J.; Yao, Y.; Gong, Y.; Kierzewski, I.; Xie, J.; Hu, L. All-Wood, Low Tortuosity, Aqueous, Biodegradable Supercapacitors with Ultra-High Capacitance. *Energy Environ. Sci.* **2017**, *10*, 538–545.
- (35) Zhou, J. H.; Sui, Z. J.; Zhu, J.; Li, P.; Chen, D.; Dai, Y. C.; Yuan, W. K. Characterization of Surface Oxygen Complexes on Carbon Nanofibers by TPD, XPS and FT-IR. *Carbon* **2007**, *45*, 785–796.
- (36) Ali, S.; Fu, L.; Lian, Z.; Li, B.; Sheng, S.; D. The Effect of Defects on the Catalytic Activity of Single Au Atom Supported Carbon Nanotubes and Reaction Mechanism for CO Oxidation. *Phys. Chem. Chem. Phys.* **2017**, *19*, 22344–22354.

(37) Imaoka, T.; Kitazawa, H.; Chun, W. J.; Yamamoto, K. Finding the Most Catalytically Active Platinum Clusters with Low Atomicity. *Angew. Chem., Int. Ed.* **2015**, *54*, 9810–9815.

(38) An, N.; Li, S.; Duchesne, P. N.; Wu, P.; Zhang, W.; Lee, J. F.; Cheng, S.; Zhang, P.; Jia, M.; Zhang, W. Size Effects of Platinum Colloid Particles on the Structure and CO Oxidation Properties of Supported Pt/Fe₂O₃ catalysts. *J. Phys. Chem. C* **2013**, *117*, 21254–21262.

(39) Dobrin, S. CO Oxidation on Pt Nanoclusters, Size and Coverage Effects: A Density Functional Theory Study. *Phys. Chem. Chem. Phys.* **2012**, *14*, 12122.

(40) Qiao, B.; Wang, A.; Yang, X.; Allard, L. F.; Jiang, Z.; Cui, Y.; Liu, J.; Li, J.; Zhang, T. Single-Atom Catalysis of CO Oxidation Using Pt₁/FeO_x. *Nat. Chem.* **2011**, *3*, 634–641.

(41) Seh, Z. W.; Kibsgaard, J.; Dickens, C. F.; Chorkendorff, I.; Nørskov, J. K.; Jaramillo, T. F. Combining Theory and Experiment in Electrocatalysis: Insights into Materials Design. *Science* **2017**, *355*, No. eaad4998.

(42) Greeley, J.; Jaramillo, T. F.; Bonde, J.; Chorkendorff, I.; Nørskov, J. K. Computational High-Throughput Screening of Electrocatalytic Materials for Hydrogen Evolution. *Nat. Mater.* **2006**, *5*, 909–913.